PHYSICAL REVIEW C **90**, 035202 (2014)

Induced polarization of Λ(1116) in kaon electroproduction

M. Gabrielyan,[10] B. A. Raue,[10,*] D. S. Carman,[30] K. Park,[21,30,†] K. P. Adhikari,[26] D. Adikaram,[26] M. J. Amaryan,[26]
S. Anefalos Pereira,[15] H. Avakian,[30] J. Ball,[6] N. A. Baltzell,[1] M. Battaglieri,[16] V. Baturin,[30] I. Bedlinskiy,[19] A. S. Biselli,[4,9]
J. Bono,[10] S. Boiarinov,[30] W. J. Briscoe,[12] W. K. Brooks,[31] V. D. Burkert,[30] T. Cao,[29] A. Celentano,[16] S. Chandavar,[25]
G. Charles,[18] L. Colaneri,[17] P. L. Cole,[13,30] M. Contalbrigo,[14] O. Cortes,[13] V. Crede,[11] A. D'Angelo,[17] N. Dashyan,[37]
R. De Vita,[16] E. De Sanctis,[15] A. Deur,[30] C. Djalali,[29] D. Doughty,[7,30] R. Dupre,[18] L. El Fassi,[26] P. Eugenio,[11] G. Fedotov,[28,29]
S. Fegan,[16] J. A. Fleming,[32] T. A. Forest,[13] B. Garillon,[18] N. Gevorgyan,[37] Y. Ghandilyan,[37] G. P. Gilfoyle,[38]
K. L. Giovanetti,[20] F. X. Girod,[30] J. T. Goetz,[25] E. Golovatch,[28] R. W. Gothe,[29] K. A. Griffioen,[36] M. Guidal,[18] L. Guo,[10]
K. Hafidi,[1] H. Hakobyan,[31] M. Hattawy,[18] K. Hicks,[25] D. Ho,[4] M. Holtrop,[23] S. M. Hughes,[32] Y. Ilieva,[29] D. G. Ireland,[33]
B. S. Ishkhanov,[28] D. Jenkins,[34] H. Jiang,[29] H. S. Jo,[18] K. Joo,[8] D. Keller,[25,35] M. Khandaker,[13,24] W. Kim,[21] F. J. Klein,[5]
S. Koirala,[26] V. Kubarovsky,[27,30] S. E. Kuhn,[26] S. V. Kuleshov,[31] P. Lenisa,[14] W. I. Levine,[4] K. Livingston,[33]
I. J. D. MacGregor,[33] M. Mayer,[26] B. McKinnon,[33] C. A. Meyer,[4] M. D. Mestayer,[30] M. Mirazita,[15] V. Mokeev,[30]
C. I. Moody,[1] H. Moutarde,[6] A. Movsisyan,[14] E. Munevar,[30] C. Munoz Camacho,[18] P. Nadel-Turonski,[30] S. Niccolai,[18]
G. Niculescu,[20,25] M. Osipenko,[16] L. L. Pappalardo,[14] R. Paremuzyan,[37,‡] E. Pasyuk,[30] P. Peng,[35] W. Phelps,[10] J. J. Phillips,[33]
S. Pisano,[15] O. Pogorelko,[19] S. Pozdniakov,[19] J. W. Price,[3] S. Procureur,[6] D. Protopopescu,[33] D. Rimal,[10] M. Ripani,[16]
A. Rizzo,[17] F. Sabatié,[6] C. Salgado,[24] D. Schott,[10,12] R. A. Schumacher,[4] A. Simonyan,[37] G. D. Smith,[32,§] D. I. Sober,[5]
D. Sokhan,[33] S. S. Stepanyan,[21] S. Stepanyan,[30] I. I. Strakovsky,[12] S. Strauch,[29] V. Sytnik,[31] W. Tang,[25] M. Ungaro,[27,30]
A. V. Vlassov,[19] H. Voskanyan,[37] E. Voutier,[22] N. K. Walford,[5] D. P. Watts,[32] X. Wei,[30] L. B. Weinstein,[26]
N. Zachariou,[29] L. Zana,[32] J. Zhang,[30] and I. Zonta[17]
(CLAS Collaboration)

[1] *Argonne National Laboratory, Argonne, Illinois 60439, USA*
[2] *Arizona State University, Tempe, Arizona 85287-1504, USA*
[3] *California State University, Dominguez Hills, Carson, California 90747, USA*
[4] *Carnegie Mellon University, Pittsburgh, Pennsylvania 15213, USA*
[5] *Catholic University of America, Washington, DC 20064, USA*
[6] *CEA, Centre de Saclay, Irfu/Service de Physique Nucléaire, 91191 Gif-sur-Yvette, France*
[7] *Christopher Newport University, Newport News, Virginia 23606, USA*
[8] *University of Connecticut, Storrs, Connecticut 06269, USA*
[9] *Fairfield University, Fairfield, Connecticut 06824, USA*
[10] *Florida International University, Miami, Florida 33199, USA*
[11] *Florida State University, Tallahassee, Florida 32306, USA*
[12] *The George Washington University, Washington, DC 20052, USA*
[13] *Idaho State University, Pocatello, Idaho 83209, USA*
[14] *INFN, Sezione di Ferrara, 44100 Ferrara, Italy*
[15] *INFN, Laboratori Nazionali di Frascati, 00044 Frascati, Italy*
[16] *INFN, Sezione di Genova, 16146 Genova, Italy*
[17] *INFN, Sezione di Roma Tor Vergata, 00133 Rome, Italy*
[18] *Institut de Physique Nucléaire ORSAY, Orsay, France*
[19] *Institute of Theoretical and Experimental Physics, Moscow, 117259, Russia*
[20] *James Madison University, Harrisonburg, Virginia 22807, USA*
[21] *Kyungpook National University, Daegu 702-701, Republic of Korea*
[22] *LPSC, Universite Joseph Fourier, CNRS/IN2P3, INPG, Grenoble, France*
[23] *University of New Hampshire, Durham, New Hampshire 03824-3568, USA*
[24] *Norfolk State University, Norfolk, Virginia 23504, USA*
[25] *Ohio University, Athens, Ohio 45701, USA*
[26] *Old Dominion University, Norfolk, Virginia 23529, USA*
[27] *Rensselaer Polytechnic Institute, Troy, New York 12180-3590, USA*
[28] *Skobeltsyn Institute of Nuclear Physics, Lomonosov Moscow State University, 119234 Moscow, Russia*
[29] *University of South Carolina, Columbia, South Carolina 29208, USA*
[30] *Thomas Jefferson National Accelerator Facility, Newport News, Virginia 23606, USA*
[31] *Universidad Técnica Federico Santa María, Casilla 110-V Valparaíso, Chile*
[32] *Edinburgh University, Edinburgh EH9 3JZ, United Kingdom*
[33] *University of Glasgow, Glasgow G12 8QQ, United Kingdom*
[34] *Virginia Polytechnic Institute and State University, Blacksburg, Virginia 24061-0435, USA*
[35] *University of Virginia, Charlottesville, Virginia 22901, USA*
[36] *College of William and Mary, Williamsburg, Virginia 23187-8795, USA*
[37] *Yerevan Physics Institute, 375036 Yerevan, Armenia*

0556-2813/2014/90(3)/035202(16)

©2014 American Physical Society

[38]*University of Richmond, Richmond, Virginia 23221, USA*

(Received 16 June 2014; revised manuscript received 21 August 2014; published 15 September 2014)

We have measured. the induced polarization of the $\Lambda(1116)$ in the reaction $ep \to e'K^+\Lambda$, detecting the scattered e' and K^+ in the final state along with the proton from the decay $\Lambda \to p\pi^-$. The present study used the CEBAF Large Acceptance Spectrometer (CLAS), which allowed for a large kinematic acceptance in invariant energy W ($1.6 \leqslant W \leqslant 2.7$ GeV) and covered the full range of the kaon production angle at an average momentum transfer $Q^2 = 1.90$ GeV^2. In this experiment a 5.50-GeV electron beam was incident upon an unpolarized liquid-hydrogen target. We have mapped out the W and kaon production angle dependencies of the induced polarization and found striking differences from photoproduction data over most of the kinematic range studied. However, we also found that the induced polarization is essentially Q^2 independent in our kinematic domain, suggesting that somewhere below the Q^2 covered here there must be a strong Q^2 dependence. Along with previously published photo- and electroproduction cross sections and polarization observables, these data are needed for the development of models, such as effective field theories, and as input to coupled-channel analyses that can provide evidence of previously unobserved s-channel resonances.

DOI: 10.1103/PhysRevC.90.035202 PACS number(s): 13.40.−f, 13.88.+e, 14.20.Gk, 14.20.Jn

I. INTRODUCTION

The strange quark plays an important role in understanding the strong interactions of the nucleon [1–3]. The investigation of strangeness production in both photo- and electroproduction reactions has been carried out since the 1970s, but there is still no comprehensive model describing the reaction mechanism. This is due, in part, to the difficulties encountered in modeling the strong interaction in the energy range of excited baryon masses. As such, the problem has been approached through the use of effective field theories [4–9], Regge models [10–12], hybrid Regge-plus-resonance (RPR) models [13,14], and more recently, through coupled-channel analyses [15–18]. All of these methods require large and precise data sets in order to constrain fitting parameters. The work presented in this paper is part of a larger program being carried out by the CLAS Collaboration at Jefferson Lab to determine cross sections and polarization observables in kaon photo- and electroproduction over a broad kinematic range, which can then be used as input to constrain the aforementioned models.

An important part of these efforts is the identification of nucleon resonances that couple to the $K^+\Lambda$ final state. Constituent quark models [19] predict the existence of excited nucleon states, many of which have yet to be observed experimentally. Many of the data on nucleon resonances come from $\pi N \to N^* \to \pi N$ reactions. However, because the density of states for this channel is high, unambiguously identifying the signal for a relatively weak or broad resonance is difficult. To fully understand the production and decay of excited baryon states, other reaction channels must be explored, such as electromagnetic production with decay via kaon emission.

Strangeness production experiments using hadronic or electromagnetic beams on various nuclear targets have been carried out since the 1970s, but only in the past decade have high-precision data on a large number of observables become available. Data on differential cross sections and spin observables for KY photoproduction have been published by the SAPHIR [20–22], LEPS [23–25], GRAAL [26–28], and CLAS [29–33] Collaborations. Together, these data cover the full range of $\cos\theta_K^{\text{c.m.}}$ and invariant energy W from 1.6 to 2.8 GeV. The recent photoproduction results from CLAS [32,33] not only extended the existing W range by 500 MeV, they significantly improved the precision of the cross section and induced hyperon polarization data. These experiments have been essential in providing evidence for new excited states in the mass range around 1900 MeV that are now included in the particle data tables [34].

High statistics data for KY electroproduction are relatively sparse as compared to photoproduction. Recently, the CLAS Collaboration published data on differential cross sections and separated structure functions for the $K^+\Lambda$ and $K^+\Sigma^0$ final states [35–37]. These data cover the full kaon center-of-mass angular range with momentum transfer Q^2 from 0.5 to 3.9 GeV^2 and W from threshold to 2.6 GeV. Differential cross sections and the separation of the longitudinal and transverse structure functions in the $ep \to e'K^+\Lambda$ and $ep \to e'K^+\Sigma^0$ reactions were published by the Jefferson Lab Hall C Collaboration [38,39]. These data cover a Q^2 range from 0.5 to 2 GeV^2 at $W = 1.84$ GeV. In a recent publication from Hall A at Jefferson Lab [40], the longitudinal, σ_L, and transverse, σ_T, structure functions were separated by the Rosenbluth technique at fixed W and t. These results cover the kinematic range for Q^2 from 1.90 to 2.35 GeV^2 and W from 1.80 to 2.14 GeV. Recent CLAS [41,42] beam-recoil polarization transfer data for the exclusive $\vec{e}p \to e'K^+\vec{Y}$ (where Y is either a Λ or Σ^0) reaction have a wide kinematic coverage spanning Q^2 from 0.7 to 5.4 GeV^2 and W from 1.6 to 2.6 GeV.

The reaction amplitude for the $K^+\Lambda$ electroproduction reaction is constructed by including the presumed contributions from the underlying resonant and nonresonant processes. The model parameters include the particular set of nucleon

---

[*]Corresponding author: baraue@fiu.edu

[†]Present address: Old Dominion University, Norfolk, Virginia 23529, USA.

[‡]Present address: Institut de Physique Nucléaire ORSAY, Orsay, France.

[§]Present address: University of Glasgow, Glasgow G12 8QQ, United Kingdom.

resonances with their respective mass, width, and electromagnetic couplings, along with the parameters that account for the nonresonant background. The parameters are then constrained by fits to the available data as a function of the relevant kinematic variables (see Refs. [4–18] for details). These fits have historically been dominated by measurements of the differential cross sections. However, polarization observables possess a strong discriminatory power that can be used for distinguishing between different theoretical models and their variants, for which the differential cross sections alone have proven to be insufficient [43]. In this paper we present results for the induced polarization of the Λ from the reaction $ep \to e'K^+\vec{\Lambda}$. These results, when added to the world's database, will help to constrain model parameters of strangeness production, which will help to better understand which N^* resonances couple to the $K^+\Lambda$ channel as well as to determine their quantum numbers, coupling strengths, masses, and widths. In addition, as these data help to constrain the available models to provide a description of all available observables (cross sections and spin observables), they will help to provide for a better understanding of the strangeness production reaction mechanism through a better understanding of the contributions of both the resonant and nonresonant amplitudes.

The organization of this paper is as follows. Section II gives the relevant formalism for the polarization observables presented in this paper. Section III contains the details of the experimental setup and describes all analysis cuts, data binning, corrections, and fitting procedures. Section IV contains a discussion of the sources of systematic uncertainty on the polarization observables. Section V contains our results and discussion. Finally, Sec. VI presents our conclusions.

TABLE I. Response functions for pseudoscalar meson electroproduction [43]. The target (recoil) polarization is related to the coordinate axes denoted by α (β) (see Fig. 1). The last three columns are for a polarized electron beam. The symbol ‡ indicates a response function that does not vanish but is related to other response functions.

β	α	T	L	${}^cLT$	${}^sLT$	${}^cTT$	${}^sTT$	${}^cLT'$	${}^sLT'$	TT'
		R_T^{00}	R_L^{00}	R_{LT}^{00}	0	R_{TT}^{00}	0	0	$R_{LT'}^{00}$	0
	x	0	0	0	R_{LT}^{0x}	0	R_{TT}^{0x}	$R_{LT'}^{0x}$	0	$R_{TT'}^{0x}$
	y	R_T^{0y}	R_L^{0y}	R_{LT}^{0y}	0	‡	0	0	$R_{LT'}^{0y}$	0
	z	0	0	0	R_{LT}^{0z}	0	R_{TT}^{0z}	$R_{LT'}^{0z}$	0	$R_{TT'}^{0z}$
x'		0	0	0	$R_{LT}^{x'0}$	0	$R_{TT}^{x'0}$	$R_{LT'}^{x'0}$	0	$R_{TT'}^{x'0}$
y'		$R_T^{y'0}$	‡	‡	0	‡	0	0	‡	0
z'		0	0	0	$R_{LT}^{z'0}$	0	$R_{TT}^{z'0}$	$R_{LT'}^{z'0}$	0	$R_{TT'}^{z'0}$
x'	x	$R_T^{x'x}$	$R_L^{x'x}$	$R_{LT}^{x'x}$	0	‡	0	0	$R_{LT'}^{x'x}$	0
x'	y	0	0	0	‡	0	‡	‡	0	‡
x'	z	$R_T^{x'z}$	$R_L^{x'z}$	‡	0	‡	0	0	‡	0
y'	x	0	0	0	‡	0	‡	‡	0	‡
y'	y	‡	‡	‡	0	‡	0	0	‡	0
y'	z	0	0	0	‡	0	‡	‡	0	‡
z'	x	$R_T^{z'x}$	‡	$R_{LT}^{z'x}$	0	‡	0	0	$R_{LT'}^{z'x}$	0
z'	y	0	0	0	‡	0	‡	‡	0	‡
z'	z	$R_T^{z'z}$	‡	‡	0	‡	0	0	‡	0

II. FORMALISM

For electroproduction, the reaction kinematics are uniquely defined by the set of four variables (Q^2, W, $\cos\theta_K^{\text{c.m.}}$, Φ), where $\theta_K^{\text{c.m.}}$ is the kaon production angle in the virtual photon-proton center-of-mass (c.m.) frame defined in Fig. 1, and Φ is the relative angle between the electron-scattering and the hadron-production planes. $Q^2 = -q^2$ is the squared four-momentum transfer of the virtual photon and $W = \sqrt{M_p^2 + 2M_p\nu - Q^2}$ is the invariant mass of the intermediate state, where M_p is the proton mass and $\nu = E_e - E_{e'}$ is the difference between the incident (E_e) and scattered ($E_{e'}$) electron energies.

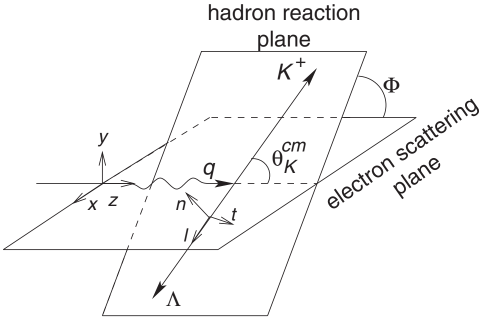

FIG. 1. Kinematics for $K^+\Lambda$ electroproduction showing the angles and polarization axes in the c.m. reference frame.

The cross sections and the polarization observables for pseudoscalar meson electroproduction can be expressed in terms of 36 nonzero response functions (see Table I) according to the framework of Ref. [43]. However, not all of these response functions are independent and a complete description of electroproduction requires only 11 independent measurements. Some of these observables have already been measured as discussed in Sec. I.

The $K^+\Lambda$ electroproduction cross section in the single-photon exchange approximation can be expressed as a product of the virtual photon flux, Γ, and the virtual photoabsorption cross section as

$$\frac{d^5\sigma}{dE_{e'}d\Omega_{e'}d\Omega_K^{\text{c.m.}}} = \Gamma\frac{d^2\sigma_v}{d\Omega_K^{\text{c.m.}}}, \tag{1}$$

where

$$\Gamma = \frac{\alpha}{4\pi}\frac{W}{M_p^2E_e^2}\left(W^2 - M_p^2\right)\left[\frac{1}{Q^2(1-\epsilon)}\right]. \tag{2}$$

Here, α is the fine-structure constant and ϵ is the virtual photon polarization parameter given by

$$\epsilon = \left[1 + 2\left(1 + \frac{\nu^2}{Q^2}\right)\tan^2\frac{\theta_{e'}}{2}\right]^{-1}, \tag{3}$$

where $\theta_{e'}$ is the scattered electron laboratory polar angle. The virtual photoabsorption cross section can be written in terms of the response functions $R_i^{\beta\alpha}$ as

$$\begin{aligned}\frac{d^2\sigma_v}{d\Omega_K^{\text{c.m.}}} = {} & K S_\alpha S_\beta \big[R_T^{\beta\alpha} + \epsilon R_L^{\beta\alpha} + \sqrt{\epsilon(1+\epsilon)} \\ & \times \big({}^c R_{LT}^{\beta\alpha} \cos\Phi + {}^s R_{LT}^{\beta\alpha} \sin\Phi \big) \\ & + \epsilon \big({}^c R_{TT}^{\beta\alpha} \cos 2\Phi + {}^s R_{TT}^{\beta\alpha} \sin 2\Phi \big) \\ & + h\sqrt{\epsilon(1-\epsilon)} \big({}^c R_{LT'}^{\beta\alpha} \cos\Phi + {}^s R_{LT'}^{\beta\alpha} \sin\Phi \big) \\ & + h\sqrt{1-\epsilon^2} R_{TT'}^{\beta\alpha} \big]. \end{aligned} \tag{4}$$

In this expression, the kinematic factor, $K = \frac{|\vec{p}_K|}{k_\gamma^{\text{c.m.}}}$, is the ratio of the kaon and virtual photon momenta in the c.m. frame and h is the electron-beam helicity. The superscripts α and β refer to the target and Λ polarizations, respectively, where a sum over α and β is implied. The c and s superscripts on the response functions refer to the cosine or sine terms that accompany them. Only one of these is nonzero for a given combination of α and β as summarized in Table I.

The spin-projection operators are defined as

$$S_\alpha = (1,\mathbf{S}),$$
$$S_\beta = (1,\mathbf{S}'),$$

with

$$\mathbf{S} = (\hat{S}_x,\hat{S}_y,\hat{S}_z),$$
$$\mathbf{S}' = (\hat{S}_{x'},\hat{S}_{y'},\hat{S}_{z'}).$$

The unprimed-coordinate system is associated with the electron-scattering plane. It is defined with the $\hat{z}$ axis along the virtual photon momentum vector $\vec{q}$, with $\hat{y}$ normal to the electron-scattering plane, and $\hat{x} = \hat{y} \times \hat{z}$. The primed-coordinate system is associated with the hadron-plane coordinates and is defined so that $\hat{z}'$ is along the kaon momentum vector $\vec{p}_K$, with $\hat{y}'$ normal to the hadron production plane, and $\hat{x}' = \hat{y}' \times \hat{z}'$.

In the simplest case, with nothing polarized, the contributions from the beam, target, and recoil polarizations vanish, and Eq. (4) reduces to

$$\begin{aligned}\sigma_0 \equiv \left(\frac{d^2\sigma_v}{d\Omega_K^{\text{c.m.}}}\right)^{00} = {} & K\big[R_T^{00} + \epsilon R_L^{00} + \sqrt{\epsilon(1+\epsilon)} R_{LT}^{00} \cos\Phi \\ & + \epsilon R_{TT}^{00} \cos 2\Phi\big], \end{aligned} \tag{5}$$

so that $K R_i^{00} = \sigma_i$ are the unpolarized cross-section components.

During this experiment, a longitudinally polarized electron beam was incident upon an unpolarized proton target, producing a polarized recoil hyperon. Summed over both helicities of the incident electron beam Eq. (4) becomes

$$\frac{d^2\sigma_v}{d\Omega_K^{\text{c.m.}}} = \sigma_0\big(1 + P_{x'}^0 \hat{S}_{x'} + P_{y'}^0 \hat{S}_{y'} + P_{z'}^0 \hat{S}_{z'}\big), \tag{6}$$

where the $P_{j'}^0$ terms (with $j' = x',y',z'$) are the induced hyperon polarization components with respect to the primed coordinate system. These components can be expressed in terms of the response functions as

$$\begin{aligned} P_{x'}^0 &= \frac{K}{\sigma_0}\big(\sqrt{\epsilon(1+\epsilon)}\, R_{LT}^{x'0} \sin\Phi + \epsilon\, R_{TT}^{x'0} \sin 2\Phi\big), \\ P_{y'}^0 &= \frac{K}{\sigma_0}\big(R_T^{y'0} + \epsilon R_L^{y'0} + \sqrt{\epsilon(1+\epsilon)}\, R_{LT}^{y'0} \cos\Phi \\ &\quad + \epsilon\, R_{TT}^{y'0} \cos 2\Phi\big), \\ P_{z'}^0 &= \frac{K}{\sigma_0}\big(\sqrt{\epsilon(1+\epsilon)}\, R_{LT}^{z'0} \sin\Phi + \epsilon\, R_{TT}^{z'0} \sin 2\Phi\big). \end{aligned} \tag{7}$$

The integration of Eq. (6) over the full Φ range, which is necessary in this experiment to reduce statistical uncertainties and to allow for finer binning in W and $\cos\theta_K^{\text{c.m.}}$, leads to

$$\begin{aligned}\int_0^{2\pi} \frac{d^2\sigma_v}{d\Omega_K^{\text{c.m.}}} d\Phi = {} & 2\pi K\big(R_T^{00} + \epsilon R_L^{00}\big) \\ & \times \big(1 + \mathcal{P}_{x'}^0 S_{x'} + \mathcal{P}_{y'}^0 S_{y'} + \mathcal{P}_{z'}^0 S_{z'}\big), \end{aligned} \tag{8}$$

where $\mathcal{P}_{j'}^0$ are Φ-integrated polarization components in the primed coordinate system,

$$\begin{aligned} \mathcal{P}_{x'}^0 &= 0, \\ \mathcal{P}_{y'}^0 &= \frac{K}{\sigma_0}\big(R_T^{y'0} + \epsilon R_L^{y'0}\big), \quad \text{and} \\ \mathcal{P}_{z'}^0 &= 0. \end{aligned} \tag{9}$$

Equations (9) show that only the normal component of the induced polarization survives the Φ integration.

The coordinate system, $(\hat{t},\hat{n},\hat{l})$, which was used in this analysis, is defined with $\hat{l}$ along the Λ momentum direction $(\hat{l} = -\hat{z}')$, $\hat{n}$ normal to the hadron plane $(\hat{n} = \hat{y}')$, and $\hat{t} = -\hat{x}'$. The polarization components in this system are given by

$$\mathcal{P}_t^0 = -\mathcal{P}_{x'}^0, \quad \mathcal{P}_n^0 = \mathcal{P}_{y'}^0, \quad \mathcal{P}_l^0 = -\mathcal{P}_{z'}^0. \tag{10}$$

III. EXPERIMENT DESCRIPTION AND DATA ANALYSIS

A. CLAS spectrometer

The CEBAF Large Acceptance Spectrometer (CLAS) [44] was designed to allow operation with both electron and photon beams, while providing an acceptance for charged particles of approximately 50% of 4π in solid angle. The large acceptance of CLAS is crucial for investigations of multiparticle final states that result from the decay of baryons and mesons.

CLAS was divided into six identical sectors by superconducting coils that produced an approximately toroidal magnetic field about the beam axis. The field was set at 60% of its maximum for this experiment. Each of the six CLAS sectors was equipped with an identical set of detectors: three layers of drift chambers (DCs) [45] for charged particle tracking and momentum reconstruction, Cherenkov counters (CCs) [46] for electron identification and triggering, scintillation counters for time-of-flight (TOF) [47] measurements and charged particle identification, and electromagnetic calorimeters (ECs) [48] for electron identification and triggering. The CLAS kinematic acceptance for this experiment was $0.8 \leqslant Q^2 \leqslant 3.5$ GeV^2 and $1.6 \leqslant W \leqslant 2.7$ GeV, with hadron scattering angles from 8° to 142° and electron scattering angles from 8° to 45°. Figure 2 illustrates a schematic view of the CLAS detector subsystems.

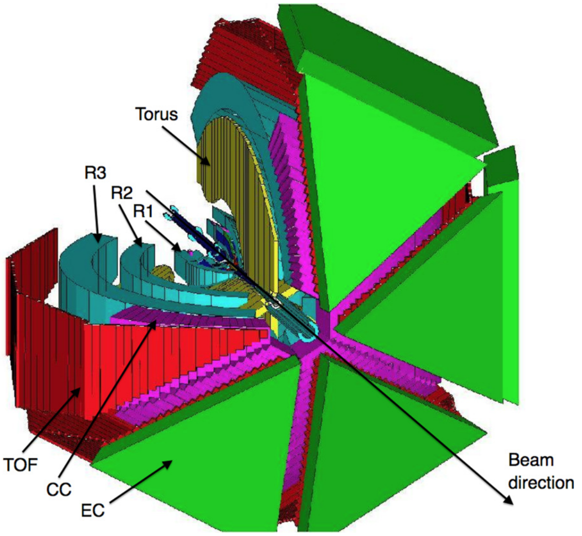

FIG. 2. (Color online) Three-dimensional cut-away view of CLAS showing the drift chambers (R1, R2, and R3), Cherenkov counters (CC), time-of-flight system (TOF), and Electromagnetic calorimeters (EC). In this view, the beam enters the picture from the upper left corner and travels down the center of the detector. The detector is roughly 10 m in diameter.

In this experiment, a 5.50-GeV longitudinally polarized electron beam with an average beam current of 7 nA was incident upon an unpolarized liquid-hydrogen target. The target was 5.0 cm long and positioned 25 cm upstream of the nominal CLAS center. The average luminosity was about 1×10^{34} cm^{-2} s^{-1}. Event readout was triggered by a coincidence between a CC hit and an EC hit in a single sector, generating an event rate of about 2 kHz. The live-time corrected integrated luminosity of this data set is 11 fb^{-1}, and the data set for this analysis contained $\sim 1 \times 10^5$ $e'K^+\Lambda$ events.

B. Event identification

The trigger configuration ensured that all events had an electron candidate. Electron candidates were also required to have a valid track in the DC corresponding to a negatively charged particle and a hit in the TOF system that coincided in time with the hit in the EC. The events for which these conditions were not satisfied were rejected in the offline analysis during event reconstruction. Additional cuts applied to improve the electron identification included geometrical fiducial cuts, which made sure that electrons hit a region of CLAS with a relatively flat acceptance, target-vertex cuts, which ensured that the scattered electron came from the target, and EC fiducial cuts, which ensured complete energy deposition in the calorimeter.

This analysis required the detection of a kaon and a proton from the Λ decay along with the electron. Hadrons were required to have a valid track in the DC corresponding to a positively charged particle and a hit in the TOF system that coincided in time. Hadrons were identified using the time-of-flight difference $\Delta t = t_1 - t_2$, where t_1 is the measured time of flight from the interaction vertex position to the hit TOF paddle and t_2 is the time for a particle with an assumed mass to travel the same distance. The time t_2 was calculated as

$$t_2 = \frac{d}{c\beta_2}, \qquad (11)$$

where d is the measured flight path length and

$$\beta_2 = \frac{p}{\sqrt{(m_2 c)^2 + p^2}}. \qquad (12)$$

Here, m_2 is the assumed particle mass and p is the measured particle momentum.

For all positive tracks, Δt was calculated three times for assumed particle masses of a pion, kaon, and proton. The mass that gave the smallest Δt was assigned to the hadron. Figures 3(a) and 3(b) show the minimum Δt vs p distributions for identified kaons and protons before any cuts, respectively. The faint horizontal bands at ±2 ns and ±4 ns in Fig. 3(b) are due to accidental tracks from different beam bunches of the accelerator. Figures 3(c) and 3(d) show the same distributions for kaons and protons, respectively, after applying the Λ missing-mass and π missing-mass-squared cuts described in the next paragraph. The application of these cuts effectively removed the accidental coincidences and most of the background in the kaon distribution, which consisted of pions and protons misidentified as kaons. As $\beta \to 1$, the pion, kaon, and proton bands started to overlap, leading to a background that was subtracted later in the analysis (see Sec. III E).

The final-state hyperons were identified using the missing-mass technique. The correlation of missing mass squared $MM^2(e'K^+p)$ vs $MM(e'K^+)$ is shown in Fig. 4(a). Figures 4(b) and 4(c) are the projections of the correlation plot onto the respective axes. Since protons will also be present from higher mass hyperon decays, those events cannot be fully eliminated from the Λ mass peak. A cut was placed on the $MM^2(e'K^+p)$ missing mass squared distribution from -0.02 to 0.07 GeV^2 [shown in red in Fig. 4(b)]. This cut was chosen so that events with either a missing pion alone or a missing pion plus a photon remain, so that the full Σ^0 peak was preserved in the hyperon mass distribution. The low-mass tail of the Σ^0 peak beneath the Λ was removed by a fitting procedure during background subtraction and the Λ yield was determined over the range shown by the red lines in Fig. 4(c). The background subtraction procedure is discussed in Sec. III E.

C. Data binning

We employed two different binning schemes for this work. In binning I shown in Table II, the data were binned in the invariant energy, W, and the cosine of the kaon production angle in the center-of-mass frame ($\theta_K^{\text{c.m.}}$), and were summed over Q^2 and Φ. The bin widths were chosen to have approximately equal statistical uncertainties in each kinematic bin. In binning II, also summed over Φ, much larger bins in W and $\cos\theta_K^{\text{c.m.}}$ were employed to study the Q^2 dependence of the polarization. Figure 5 shows the kinematic extent of the $K^+\Lambda$ data in terms of Q^2 vs W. The Q^2 range spanned by the data depends strongly on W.

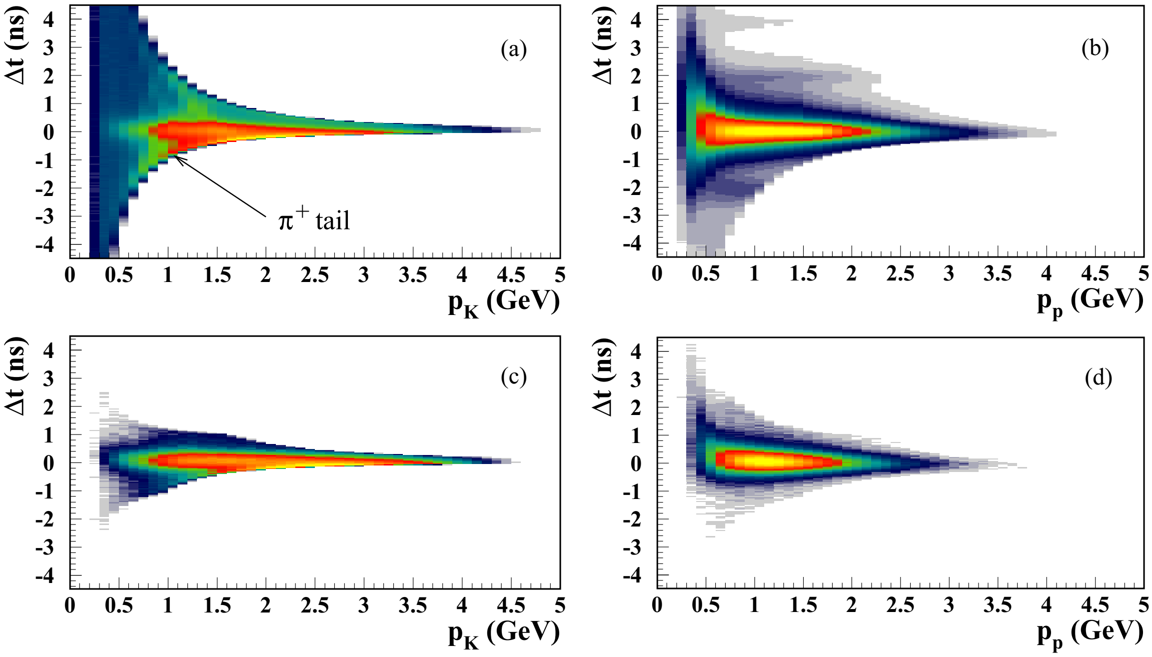

FIG. 3. (Color online) Minimum Δt (ns) vs p (GeV) distributions for identified kaons (left) and protons (right). Plots (a) and (b) show the distributions without any cuts. Plots (c) and (d) show the same distributions for kaons and protons after applying the Λ missing-mass and the π missing-mass-squared cuts shown in Fig. 4.

D. Λ polarization extraction

Although the Λ is produced in a strong hadronization process it can only decay weakly. The main decay modes of the Λ are $p\pi^-$ and $n\pi^0$ with branching ratios of 64% and 36%, respectively [34]. The Φ-integrated proton angular distribution from the Λ decay in the Λ rest frame is given by

$$\frac{dN}{d\cos\theta_p^{RF}} = N_0\left(1 + \alpha\mathcal{P}_j\cos\theta_p^{RF}\right), \tag{13}$$

where $\mathcal{P}_j$ is the Φ-integrated polarization of the Λ for an arbitrary coordinate $(\hat{t}, \hat{n}, \hat{l})$ in the Λ rest frame, θ_p^{RF} is the angle of the decay proton relative to the respective $\hat{t}$, $\hat{n}$, or $\hat{l}$ axis in the Λ rest frame, and $\alpha = 0.642 \pm 0.013$ [34] is the weak decay asymmetry parameter. The uncertainty in α is treated as a systematic uncertainty in the final result.

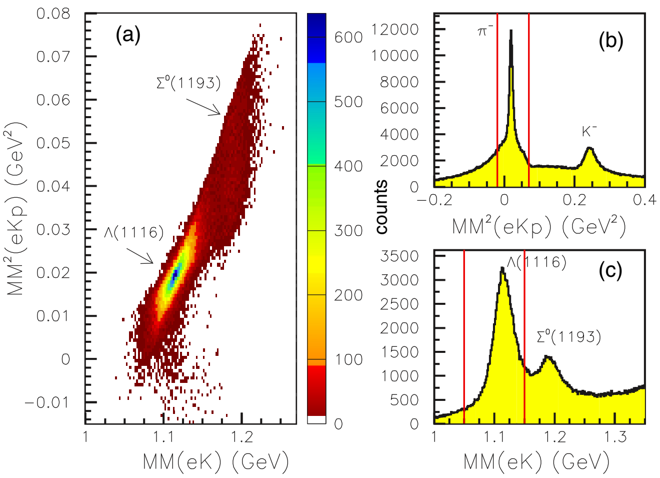

FIG. 4. (Color online) (a) Reconstructed missing mass squared $MM^2(e'K^+p)$ (GeV^2) vs baryon missing mass $MM(e'K^+)$ (GeV). (b) Missing mass squared distribution $MM^2(e'K^+p)$ (GeV^2). The red lines show the applied cut, which includes events with only a missing pion (Λ events) and events with a missing pion plus a photon (Σ^0 events). Negative values are due to finite resolution effects. (c) Hyperon missing mass $MM(e'K^+)$ distribution after applying the π missing-mass-squared cut. The red lines in this plot show the missing mass range over which the background-subtracted yields are integrated for the final Λ sample selection. All plots require a detected proton.

TABLE II. Data binning for the induced Λ polarization analysis. Binning I is used to study the W and $\cos\theta_K^{\text{c.m.}}$ dependencies and binning II is used to study the Q^2 dependence.

Variable	Range	No. of bins	Bin width
	Binning I		
$\cos\theta_K^{\text{c.m.}}$	$(-1.0, 0.0)$	2	0.5
	$(0.0, 1.0)$	5	0.2
W	1.6–2.1 GeV	20	25 MeV
	2.1–2.7 GeV	12	50 MeV
	Binning II		
$\cos\theta_K^{\text{c.m.}}$	$(-1.0, 0.0)$	1	1.
	$(0.0, 0.4)$	1	0.4
	$(0.4, 0.8)$	1	0.4
	$(0.8, 1.0)$	1	0.2
W	1.6–2.4 GeV	4	200 MeV
Q^2	0.8–3.2 GeV^2	4	0.6 GeV^2

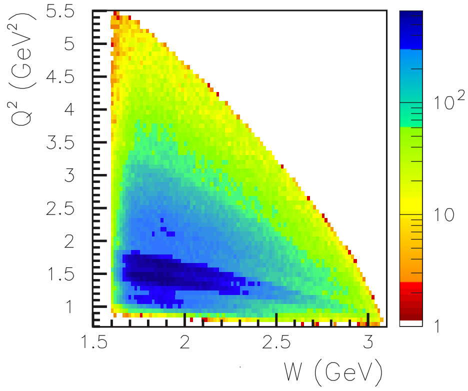

FIG. 5. (Color online) Distribution of $K^+\Lambda$ events in Q^2 and W. The $\mathcal{P}_N^0$ values are measured for W up to 2.7 GeV only and summed over the full Q^2 range.

The induced polarization for a given coordinate can be extracted by forming the forward-backward yield asymmetry with respect to $\cos\theta_p^{RF} = 0$. Integrating Eq. (13) from 0 to 1 (forward) and -1 to 0 (backward) gives the corresponding yields N^+ and N^- as

$$
\begin{aligned}
N^+ &= \int_0^1 N_0\left(1 + \alpha\mathcal{P}_j^0 \cos\theta_p^{RF}\right) d\cos\theta_p^{RF} \\
&= N_0 + N_0\frac{\alpha\mathcal{P}_j^0}{2}, \\
N^- &= \int_{-1}^0 N_0\left(1 + \alpha\mathcal{P}_j \cos\theta_p^{RF}\right) d\cos\theta_p^{RF} \\
&= N_0 - N_0\frac{\alpha\mathcal{P}_j^0}{2}.
\end{aligned}
\tag{14}
$$

The forward-backward yield asymmetry with respect to a given axis $j = (\hat{t},\hat{n},\hat{l})$, A_j, is then defined as

$$
A_j = \frac{N^+ - N^-}{N^+ + N^-} = \frac{\alpha\mathcal{P}_j^0}{2}, \tag{15}
$$

and the induced polarization can be expressed in terms of the asymmetry as

$$
\mathcal{P}_j^0 = \frac{2A_j}{\alpha} = \frac{2}{\alpha}\frac{N^+ - N^-}{N^+ + N^-}. \tag{16}
$$

E. Background subtraction

In order to form the forward-backward yield asymmetries, the background-subtracted Λ yields must be determined from the $e'K^+$ missing mass distributions. To determine the Λ yields, the contributions of background beneath the Λ peak had to be accounted for. This included the background both from the low-mass tail of the Σ^0 peak and from hadron misidentification. The respective yields of Λ, Σ^0, and other background were determined by a fit to the missing mass distributions for each kinematic bin. The Λ and Σ^0 peaks were fit with functional forms, f_Λ and f_Σ, respectively, that were motivated by the results of a Monte Carlo simulation that was well matched to the data. The simulation suggested that the line shape for each of the hyperons was well represented by a Gaussian plus two Lorentzians for the high and low mass sides of the peaks. This form accounted for the finite detector resolution, as well as the radiative tail on the high mass side of the peak. The background beneath the hyperons was primarily from pions misidentified as kaons and depended strongly on kinematics. To define the shape of this background, f_{BG}, templates were generated from the data by intentionally misidentifying pions as kaons. The scale for the background template was allowed to float as a free parameter in the fitting procedure.

The total fit function was then defined as

$$
F_{\text{TOTAL}} = f_\Lambda + f_\Sigma + f_{BG}, \tag{17}
$$

with

$$
\begin{aligned}
f_\Lambda &= G_\Lambda + L_\Lambda^L + L_\Lambda^R, \\
f_\Sigma &= G_\Sigma + L_\Sigma^L + L_\Sigma^R, \\
f_{BG} &= C_{BG} \times \text{(background template)},
\end{aligned}
$$

in which G, L^L, and L^R are the Gaussian and the left and right Lorentzian functions (low and high mass sides), respectively, and C_{BG} is the amplitude parameter for the background from hadron misidentification.

Several constraints were applied to the fits. The high and low-mass Lorentzians were required to have the same magnitude at the peak of the hyperon. The centroids of the Gaussians and Lorentzians were restricted to the PDG values of the hyperon masses [34]. To further constrain the fits, we assumed that the shape parameters (Gaussian and Lorentzian widths) must vary smoothly from one kinematic bin to the next and that the shape of the peaks must be the same for forward-going and backward-going protons in the hyperon rest frame. We parametrized the shape parameters as a function of W, thereby reducing the number of free parameters in the final fit to six for each of the backward and forward yields, where only the Gaussian and Lorentzian amplitudes were allowed to vary freely. Typical sample fits are shown in Fig. 6. The average χ^2 per degree of freedom, χ^2/ndf, was approximately 1.

The number of Λ's in each kinematic bin, corresponding to forward and backward-going protons, was determined by integrating the functions corresponding to the Λ peak within the missing mass range from 1.05 to 1.15 GeV. The background-subtracted yields, $Y_\pm$, have a statistical uncertainty given by

$$
\delta Y_\pm^2 = \sum_i^n \sum_j^n \frac{\partial f_\Lambda}{\partial a_i}\frac{\partial f_\Lambda}{\partial a_j}\epsilon_{ij}, \tag{18}
$$

where n is the number of free parameters, ϵ_{ij} is the correlation matrix from the fit, a_i and a_j are the fit parameters, and f_Λ is the Λ peak fit function integrated within the missing mass range.

F. Acceptance corrections

The final background-subtracted forward/backward yields were corrected for acceptance and efficiency effects using a GEANT-based Monte Carlo simulation. In the first stage of the simulation, $ep \to e'K^+\Lambda$ events were generated with a t-slope-modified phase-space generator. The event

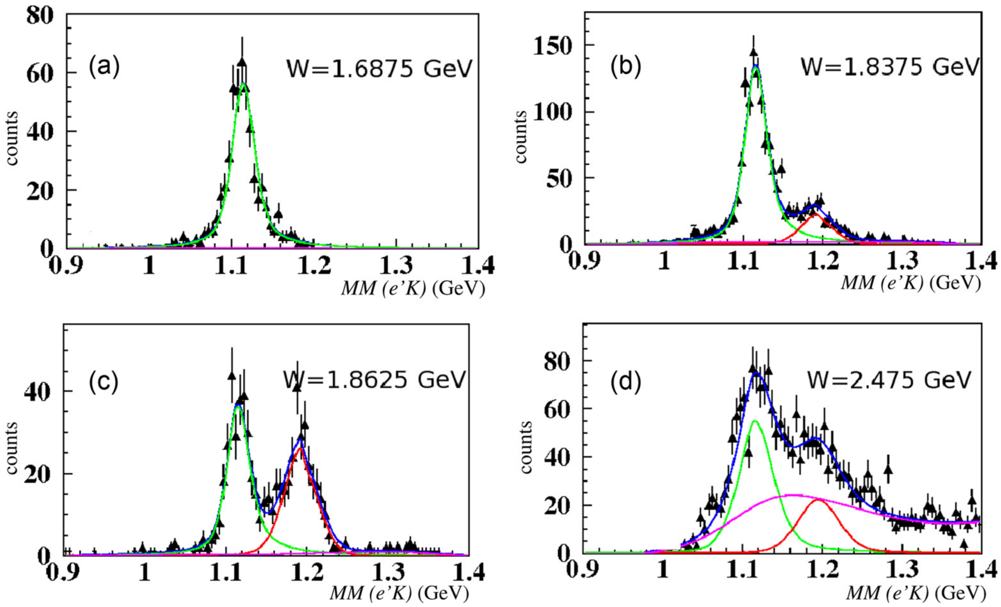

FIG. 6. (Color online) Typical fits to the reconstructed hyperon mass spectra for different W bins summed over Q^2 using Eq. (17). Panels (a)–(d) correspond to $\cos\theta_K^{\text{c.m.}} = 0.5, 0.9, 0.1$, and 0.9, respectively. The green curves correspond to the Λ peak, the red curves to Σ^0 peak, the magenta curves to the hadron-misidentification background, and the blue curves to the total fit function.

generator scaled the phase space cross section by a factor of e^{-bt}, where b is the t-slope parameter, and the Mandelstam variable $t = (k_\gamma - p_K)^2$ is the square of the difference between the virtual photon and kaon four-momenta. The choice of $b = 0.3\ \text{GeV}^{-2}$ yielded a distribution that was a reasonable match to the data. The generated events were then processed with the GSIM package, which is the GEANT simulation of the CLAS detector. Although only the external final-state radiative effects were included in GSIM, any electron or kaon radiative effects are the same for forward- and backward-going protons from the decay of the Λ and will cancel out in the forward-backward asymmetry.

In the first iteration of the simulation-based calculation of the acceptance correction, the induced polarization was assumed to be zero, leading to a uniform proton distribution in θ_p^{RF}. The particles were then propagated through CLAS and the detector response was recorded in the same way as for the experimental data. The GSIM simulation assumed a perfect detector system, so the known inefficiencies and the resolutions of the different detector components were taken into account in the next step by the GSIM post-processing (GPP) package, which smeared the DC and TOF resolutions to match the experimental data. The simulated data were processed identically to the experimental data.

The acceptance factors in this analysis were defined as the ratio of the reconstructed events to the generated events in the same kinematic bin. Two acceptance factors $f_\pm$ were defined in each kinematic bin corresponding to forward- and backward-going protons with respect to a given spin quantization axis in the Λ rest frame and are given by

$$f_\pm = \frac{N^\pm_{\text{Detected}}}{N^\pm_{\text{Thrown}}}. \tag{19}$$

The numerator, $N^\pm_{\text{Detected}}$, is the number of detected Λs after all cuts were applied and $N^\pm_{\text{Thrown}}$ is the number of generated events.

In the second iteration of the acceptance correction procedure, the induced polarization results determined using the correction factors of the zero-polarization Λ-decay simulation were then used as the input polarization of the simulated data. This gave a more realistic decay-proton distribution. The acceptance factors were then recalculated and applied to the uncorrected data yields. The change in the measured polarizations from the first to the second iteration were much smaller than the statistical uncertainties so no further iterations were done.

The W dependence of the acceptance factors are plotted in Fig. 7 for the most forward kaon angular bin. As can be seen from the plot, the normal component of the polarization has nearly identical acceptances for both forward- and backward-going protons, while the other two components have some rather large differences in the forward and backward acceptances and are therefore more sensitive to acceptance effects. This statement is true for all $\cos\theta_K^{\text{c.m.}}$ angles. As previously mentioned, the $\hat{t}$ and $\hat{\ell}$ components (see Fig. 1) of the induced polarization must vanish when integrated over Φ, which will only happen if the acceptance factors for these components are properly accounted for (see Sec. IV).

The acceptance-corrected yields for the forward and backward directions are given by

$$N_\pm = Y_\pm / f_\pm. \tag{20}$$

Here, $Y_\pm$ is the background-subtracted, uncorrected yield, obtained by fitting as described in the previous section and $f_\pm$ is the acceptance correction factor from Eq. (19) after applying the second iteration of acceptance corrections.

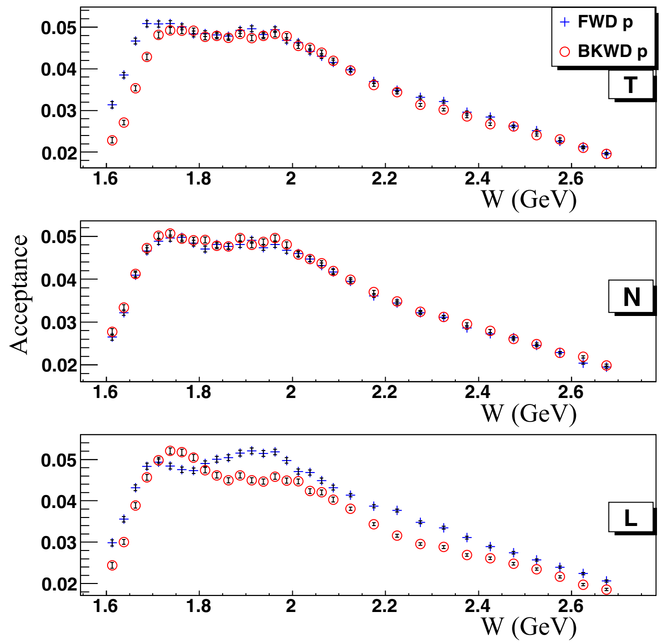

FIG. 7. (Color online) Dependence of the acceptance factors on W for forward-going (blue crosses) and backward-going (red circles) protons at $0.8 < \cos\theta_K^{\text{c.m.}} < 1$ with respect to the $\hat{t}$, $\hat{n}$, and $\hat{l}$ polarization axes.

IV. SYSTEMATIC UNCERTAINTIES

There were four primary sources of point-to-point systematic uncertainties that we identified in this analysis. These sources were from background subtraction, acceptance corrections, geometrical fiducial cuts, and hyperon peak fitting. The systematic uncertainties were determined for each source by comparing the nominal polarization results in each $\cos\theta_K^{\text{c.m.}}$ kinematic bin to the results obtained with alternative cuts or corrections. The systematic uncertainties were estimated as the uncertainty-weighted average polarization difference defined by

$$\delta P = \sqrt{\frac{\sum_{i=1}^{n} \frac{\left[P_i^{\text{nom}} - P_i^{\text{alt}}\right]^2}{\left(\delta P_i^{\text{nom}}\right)^2}}{\sum_{i=1}^{n} \frac{1}{\left(\delta P_i^{\text{nom}}\right)^2}}}. \tag{21}$$

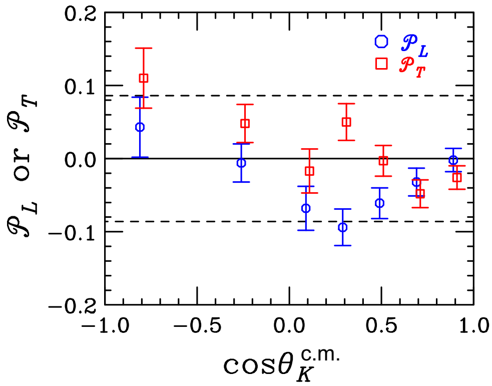

FIG. 8. (Color online) W averaged $\mathcal{P}_L^0$ (blue circles) and $\mathcal{P}_T^0$ (red squares) values vs $\cos\theta_K^{\text{c.m.}}$ summed over Q^2. The dashed lines represent the lowest total point-to-point systematic uncertainty from Table III.

Here the summation goes over all W points for each $\cos\theta_K^{\text{c.m.}}$ bin. We found that within a given $\cos\theta_K^{\text{c.m.}}$ bin, variations with W were statistically distributed.

The systematic uncertainties from all sources are detailed in Table III. Uncertainties associated with the background subtraction were determined by widening the cut on $MM^2(e'K^+p)$, thus letting in more background. The estimated background-related uncertainty is between 0.025 and 0.047. The acceptance correction uncertainty was determined by varying the t slope of the event generator over the range 0.1 to 1.0 GeV^{-2}. The estimated acceptance-correction uncertainty was between 0.063 and 0.082. The geometrical fiducial cuts on the proton acceptance were varied between tighter and looser cuts over a sensible range, leading to an estimated systematic uncertainty between 0.015 and 0.051. We tested different methods of fitting the hyperon spectrum including using different types of fitting routines and allowing shape parameters to float freely as opposed to using smoothly varying shape parameters. The estimated fitting uncertainty varied between 0.032 and 0.058.

We generally see that the systematic uncertainties get bigger at larger kaon angles. These bins have the largest statistical uncertainties and therefore estimating systematic uncertainties becomes less certain. The overall systematic uncertainty, formed from a quadrature sum of the first four sources listed in Table III, varies between 0.086 in the most forward kaon-angle bin to 0.120 at the most backward kaon-angle bin.

TABLE III. Estimated systematic uncertainties. The total point-to-point systematic uncertainty on the measured Λ induced polarization (last row) is the quadrature sum of the individual contributions.

Systematic uncertainties							
Source \ $\cos\theta_K^{\text{c.m.}}$	(−1.0,−0.5)	(−0.5,0.0)	(0.0,0.2)	(0.2,0.4)	(0.4,0.6)	(0.6,0.8)	(0.8,1.0)
Background subtraction	0.042	0.025	0.047	0.036	0.046	0.041	0.033
Acceptance corrections	0.082	0.074	0.072	0.080	0.079	0.069	0.063
Geometrical fiducial cut	0.051	0.030	0.031	0.025	0.015	0.032	0.032
Fitting	0.056	0.058	0.056	0.041	0.034	0.032	0.034
$\delta\alpha/\alpha$	0.020	0.020	0.020	0.020	0.020	0.020	0.020
Total point-to-point	0.120	0.103	0.108	0.101	0.100	0.093	0.086

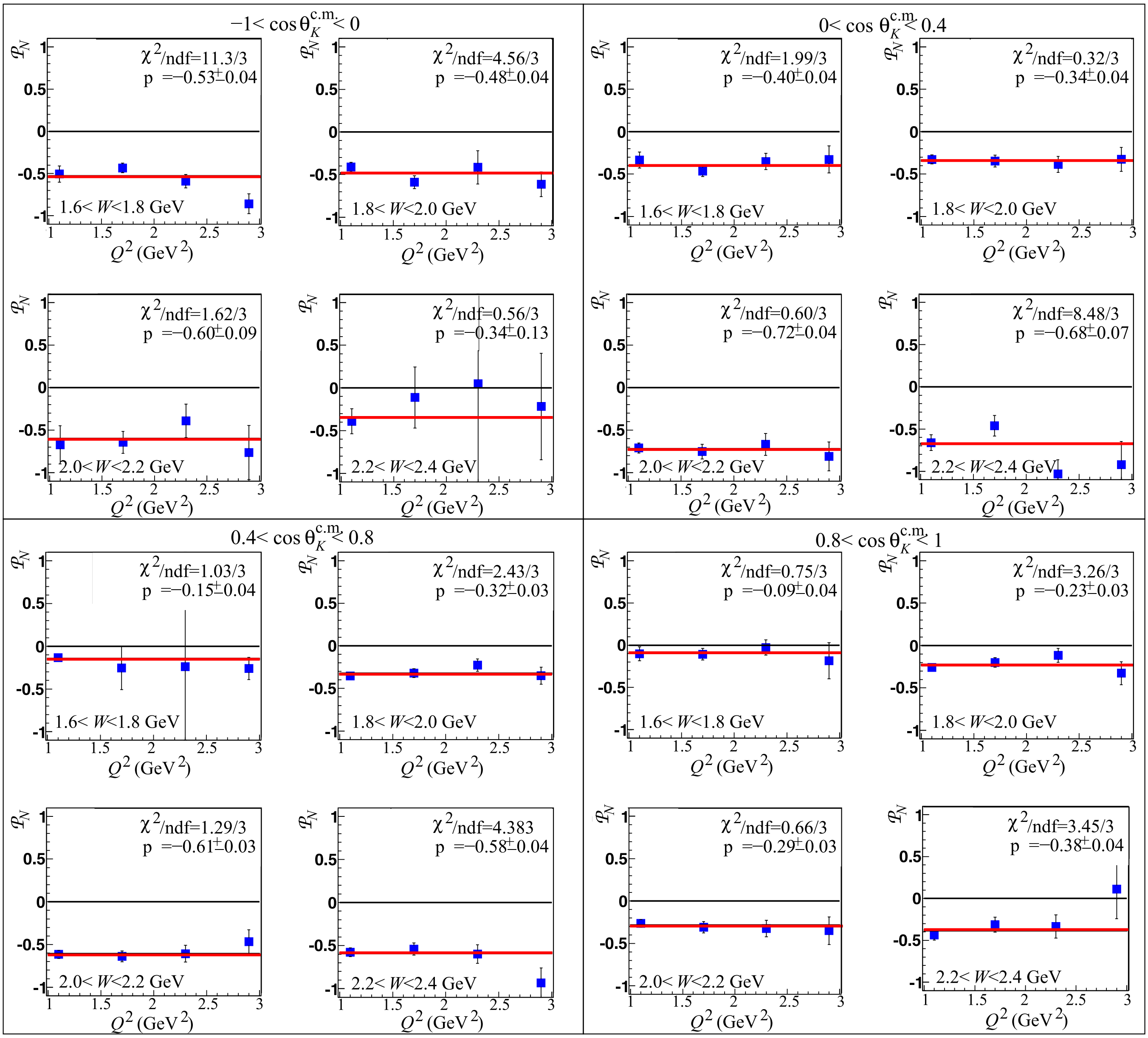

FIG. 9. (Color online) Induced Λ polarization $\mathcal{P}_N^0$ vs Q^2 for different $\cos\theta_K^{\text{c.m.}}$ and W bins. The solid red lines are fits to a constant, and the error bars are statistical only. The results show no significant dependence on Q^2 within our statistical uncertainties.

A powerful check of our systematic uncertainties was the measurement of the Φ-integrated longitudinal and transverse induced polarization components, $\mathcal{P}_L^0$ and $\mathcal{P}_T^0$. Both of these quantities should be zero according to Eq. (9). The W-averaged deviations from zero along with their uncertainties are plotted vs $\cos\theta_K^{\text{c.m.}}$ in Fig. 8 for both $\mathcal{P}_L^0$ and $\mathcal{P}_T^0$. Within statistical uncertainties all $\mathcal{P}_L^0$ and $\mathcal{P}_T^0$ fall within the range of our smallest point-to-point systematic uncertainty given by the dashed lines in the figure.

Finally, there is a scale-type uncertainty from the uncertainty on the Λ decay parameter, α. This relative uncertainty is 0.020.

V. RESULTS AND DISCUSSION

A. Q^2 dependence

Figure 9 shows the induced Λ polarization $\mathcal{P}_N^0$ vs Q^2. The data show a flat Q^2 dependence indicated by the quality of the constant fits. The largest deviation from a flat distribution is in the bin for $-1 < \cos\theta_K^{\text{c.m.}} < 0$ and $1.6 < W < 1.8$ GeV, which has a $\chi^2/ndf = 3.8$ and is essentially driven by a single data point. We will discuss implications of the Q^2 dependence later. We took advantage of this flat behavior and summed over Q^2 in order to improve the statistical precision of the data for the W and $\cos\theta_K^{\text{c.m.}}$ study.

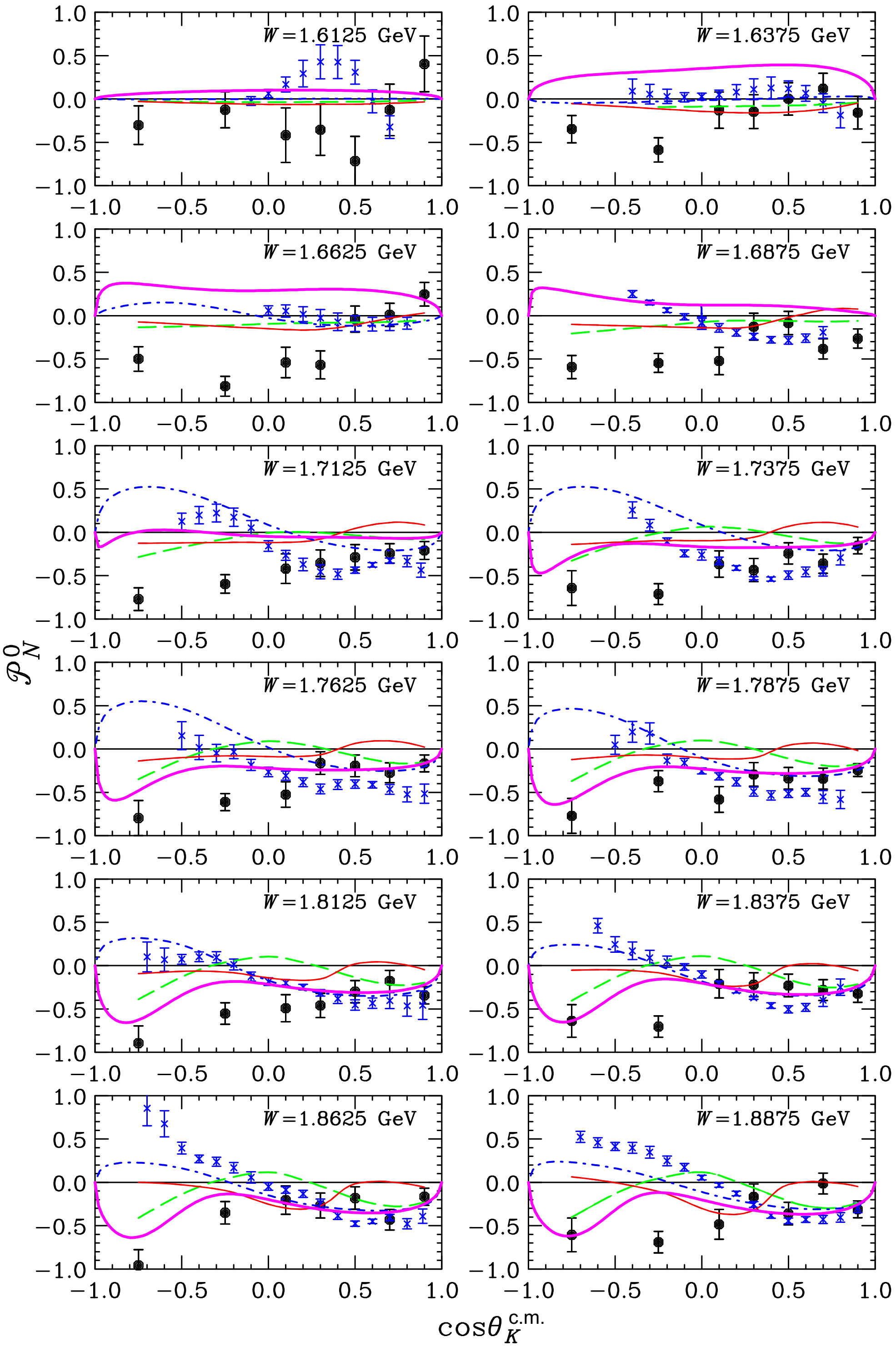

FIG. 10. (Color online) Induced Λ polarization $\mathcal{P}_N^0$ vs $\cos\theta_K^{\mathrm{c.m.}}$ for W from 1.6125 to 1.8875 GeV at an average Q^2 of 1.90 GeV^2. The black circles are the results of this analysis and the blue crosses are the CLAS photoproduction results from Ref. [32]. All data points show statistical uncertainties only. The overlaid curves correspond to RPR-2007 [13] (green long dash), RPR-2011 [14] (red solid), Extended Kaon-Maid [52] (blue dot-dash), and Maxwell [8,9] (magenta thick solid) model predictions, respectively.

B. W and $\cos\theta_K^{\mathrm{c.m.}}$ dependence

The W and $\cos\theta_K^{\mathrm{c.m.}}$ dependence of our final data are shown in Figs. 10–13 and are available through the CLAS physics database [49]. The results are presented at the geometrical bin centers and not the event-weighted average of the points. We found that the event-weighted average of W is identical to the geometrical bin centers to within three significant figures,

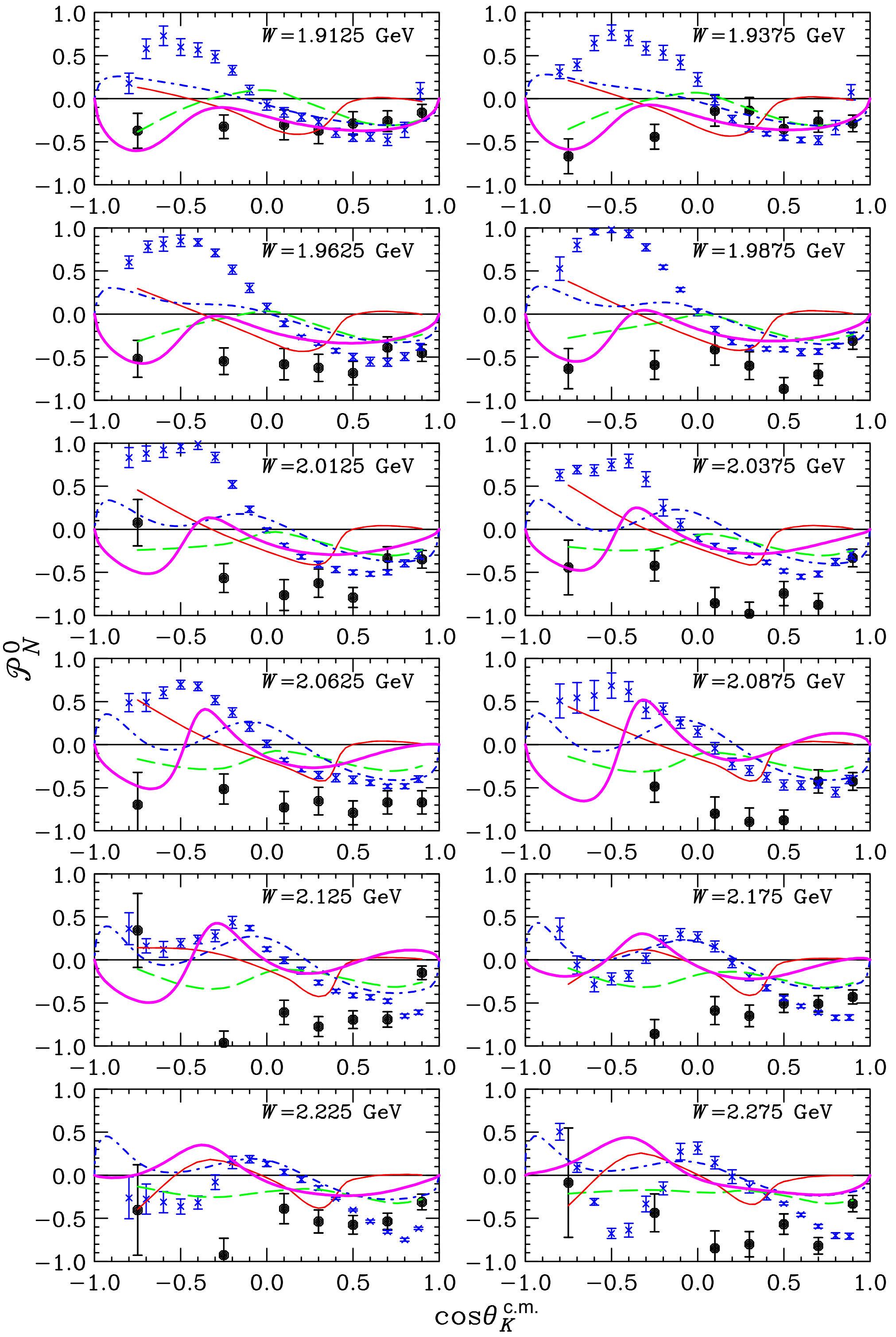

FIG. 11. (Color online) Same as Fig. 10 except for W from 1.9125 to 2.275 GeV.

while the event-weighted average of $\cos\theta_K^{\text{c.m.}}$ is generally within ±0.02 of the geometrical bin centers.

Figures 10–12 show the induced Λ polarization as a function of $\cos\theta_K^{\text{c.m.}}$ along with previous CLAS photoproduction data [32]. The average systematic uncertainty on the photoproduction points is 0.05. Our electroproduction results are persistently negative, whereas the photoproduction data are generally positive at backward kaon angles ($\cos\theta_K^{\text{c.m.}} < 0$) and negative only for forward kaon angles. The photoproduction and electroproduction data agree reasonably well for $\cos\theta_K^{\text{c.m.}} > 0.5$ where t-channel processes dominate, suggesting a dominant influence of the transverse component

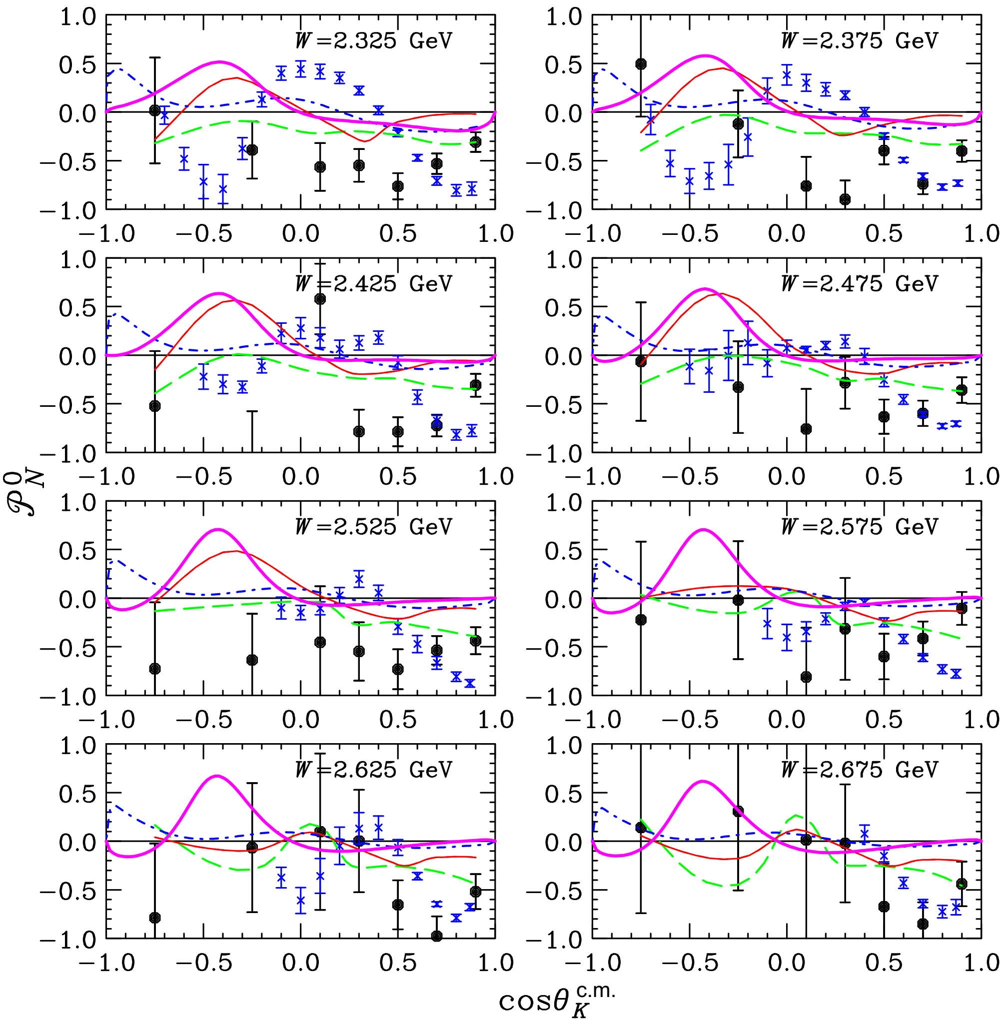

FIG. 12. (Color online) Same as Fig. 10 except for W from 2.325 to 2.675 GeV.

of the virtual photon. Previous electroproduction results from CLAS [35,37,50] showed that σ_L is small in this kinematic range, even at backward kaon angles. However, the large difference between the photo- and electroproduction results seen here suggests that although the longitudinal polarization of the virtual photon by itself may not play a significant role, even a small contribution in the interference terms may cause a sizable contribution for this observable. Furthermore, although we found a negligible Q^2 dependence in our data, the large differences between the electroproduction and photoproduction data suggests that somewhere below our lower Q^2 limit (0.8 GeV^2) there must be a dramatic change in the electroproduction values of $\mathcal{P}_N^0$.

Figure 13 shows the W dependence of $\mathcal{P}_N^0$ for all $\cos\theta_K^{\text{c.m.}}$ bins. For the two most forward kaon-angle bins, the variation with W is smooth, with no discernible fluctuations other than the monotonic decrease with increasing W. This is consistent with t-channel dominance. Another feature is that beyond about 2.1 GeV the polarization is essentially constant at a value of −0.5. In the bins from $0 < \cos\theta_K^{\text{c.m.}} < 0.6$ there is a noticeable fluctuation near 1.9 GeV. A resonance structure around 1.9 GeV has been observed in the photoproduction cross section [20,29,30,32], as well as in electroproduction measurements of $\sigma_T + \epsilon\sigma_L$ [35,37] and $\sigma_{LT'}$ [36]. Early work by Bennhold and Mart [5] explained this by postulating contributions from a previously unseen $J^P = 3/2^-$ resonance at 1.96 GeV, although subsequent models and partial wave analyses [6,15] come to different conclusions. The PDG [34] now lists a three-star, $J^P = 3/2^+$ resonance that arose from the coupled-channel analysis of Ref. [15]. Inclusion of our new induced polarization data in models will be important to better understand the contributing N^* states and their coupling parameters.

C. Comparison to theoretical models

Our polarization results are compared to three different models. One is a Regge plus resonance model (RPR) shown with two variants in Figs. 10–12, referred to here as RPR-2007 [13] and RPR-2011 [14]. Figure 13 also includes two additional variants [51], which are the RPR-2011 model with the resonances turned off, referred to here as RPR-2011NoRes, and the RPR-2011 model with $\epsilon = 0$ [effectively turning off the longitudinal response function in Eq. (9)], referred to here

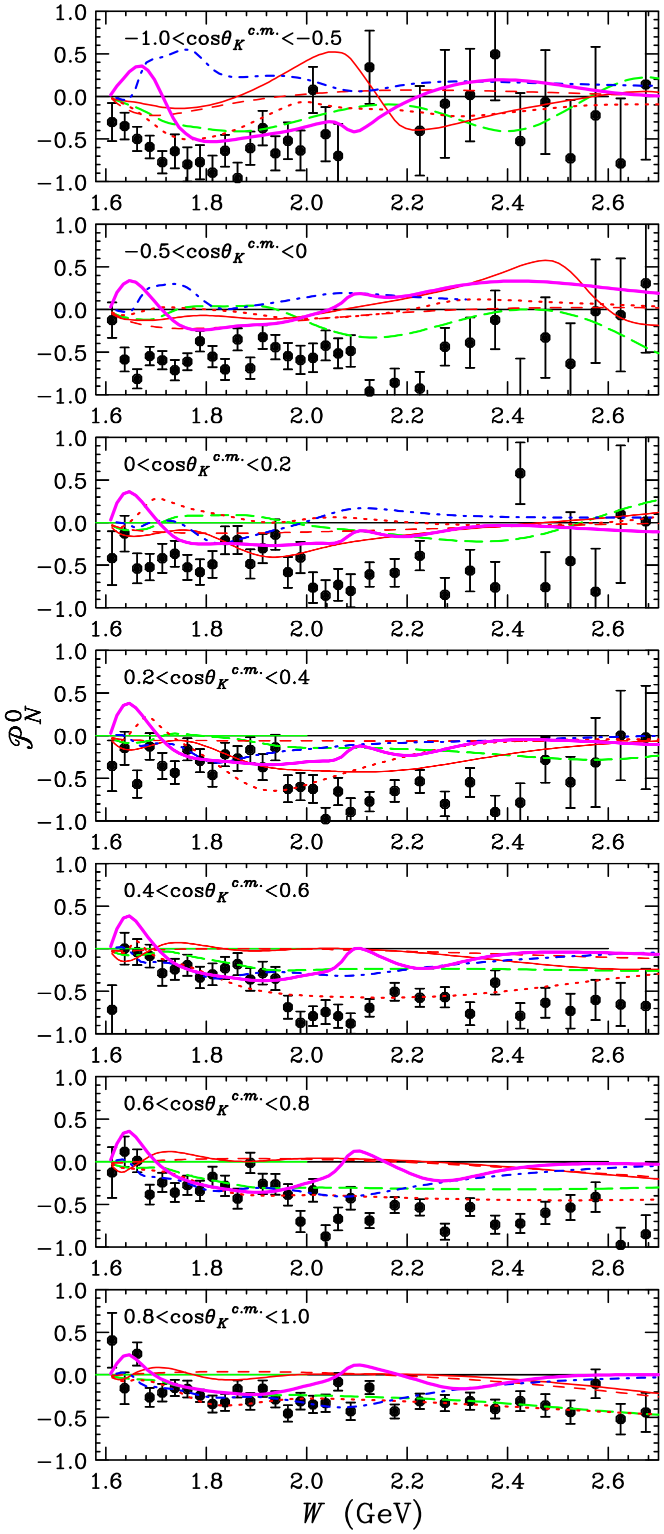

FIG. 13. (Color online) Induced Λ polarization $\mathcal{P}_N^0$ vs W for our seven $\cos\theta_K^{\mathrm{c.m.}}$ bins at an average Q^2 of 1.90 GeV^2. The symbols and curves are the same as Fig. 10 with additional curves RPR-2011NoRes (red short dash) and RPR-2011NoL (red dots) [51].

as RPR-2011NoL. The RPR model treats the nonresonant background contributions as exchanges of kaonic Regge trajectories in the t channel, with the K and K^* as the dominant trajectories. To take into account the s-channel contributions, the RPR models include established s-channel nucleon resonances: $N(1650)1/2^-$, $N(1710)1/2^+$, $N(1720)3/2^+$, as well as the $N(1900)3/2^+$. The older RPR-2007 model was fit to forward-angle ($\cos\theta_K^{\mathrm{c.m.}} > 0$) photoproduction data from CLAS, LEPS, and GRAAL [13]. The newer RPR-2011 model was fit to the entire $\cos\theta_K^{\mathrm{c.m.}}$ angular range of all recent $K^+\Lambda$ photoproduction data, including Ref. [32]. Furthermore it uses a consistent formalism for the description of spin-5/2 particles as described in Ref. [14]. Neither version of the RPR model included any fits to the existing electroproduction data.

The older RPR-2007 model does a good job of describing the data for $0.8 < \cos\theta_K^{\mathrm{c.m.}} < 1$ over the entire W range (see Fig. 13) with reasonable agreement at $-1 < \cos\theta_K^{\mathrm{c.m.}} < -0.5$ but generally fails elsewhere. At backward angles it tends to fall somewhere between the photo- and electroproduction data. The RPR-2011 model is nearly zero for the three forward angle bins and has the wrong sign for a large portion of the back-angle bins. The only bin in which it seems to have any predictive power is for $0.2 < \cos\theta_K^{\mathrm{c.m.}} < 0.4$. It was already noted in Ref. [37] when comparing the RPR-2007 and RPR-2011 models to the separated structure functions ($\sigma_T + \epsilon\sigma_L$, σ_{TT}, σ_{LT}, and $\sigma_{LT'}$) from this same data set, the RPR-2011 model fares noticeably worse than the RPR-2007 model over all angles for $W < 2.1$ GeV.

To see the effect of resonances on the calculation of this observable, Fig. 13 shows a version of RPR-2011 with the resonances turned off, RPR-2011NoRes. Except in the three back-angle bins we see little difference between RPR-2011 and RPR-2011NoRes. Since the model assumes t-channel dominance, this is not surprising. Generally speaking, however, turning off the resonances effectively drives the calculation to near zero everywhere.

Figure 13 also includes the RPR-2011 calculation without inclusion of the longitudinal response function $R_L^{y'0}$. Interestingly, it shows better overall agreement with the data than the full version of RPR-2011. This suggests that the magnitude of the longitudinal response is too large in RPR-2011 and is effectively canceling out the transverse response. Why the inclusion of spin-5/2 states and/or the back-angle CLAS photoproduction data in the evolution from RPR-2007 to RPR-2011 would cause this is something that the model builders will have to address. Clearly, the inclusion of these electroproduction data into their model should provide a better constraint on the longitudinal response.

The second model we compare our data to is the Extended Kaon-Maid model [52], which was originally compared to the low Q^2 $K^+\Lambda$ and $K^+\Sigma^0$ data of Ref. [53]. Kaon-Maid [5] is an effective field theory that includes kaon resonances $K^*(892)$ and $K_1(1270)$ in the t-channel, as well as nucleon resonances $N(1650)1/2^-$, $N(1710)1/2^+$, $N(1720)3/2^+$, and $N(1895)3/2^-$, and the extended version used here also includes $N(1675)5/2^-$, $N(1700)3/2^-$, $N(2000)5/2^+$, and $N(2200)5/2^-$ (no longer listed in the PDG). The Extended Kaon-Maid model generally agrees with the data at forward angles but shows progressively worse agreement with the data as the kaon c.m. angle increases.

Finally, we also include the effective field theory model of Maxwell [8,9]. This model was fit to all available photo- and electroproduction data (prior to 2012) up to $W = 2.3$ GeV. This model includes contributions from the t channel [$K^*(892)$ and $K_1(1270)$], all three and four star s-channel resonances up to spin 5/2 from 1440 to 2000 MeV, and several three and four star u-channel resonances with spin up to 5/2. For the range $1.75 \leqslant W \leqslant 1.95$ GeV, this model fairly accurately predicts the observed $\cos\theta_K^{\text{c.m.}}$ dependence of the data (see Figs. 10 and 11). However, outside of this narrow range, the model has some fairly obvious deficiencies. The model predicts a positive bump near threshold, which grows with angle but is not seen in the data. The model also predicts a fairly prominent bump at around 2.1 GeV (see Fig. 13), which is not seen in the data. This is likely due to the inclusion of two resonances [$N(2080)3/2^-$ and $N(2200)5/2^-$] that have recently been removed from the PDG. This model has been shown to demonstrate a similarly flat dependence on Q^2 as is seen in our data [54], yet it accurately predicts the results from photoproduction [7]. We are currently working with Maxwell to understand the Q^2 evolution of the induced polarization.

None of the available models does a satisfactory job of describing the induced Λ polarization over the full range of kinematics for our data, especially at the backward angles where s-channel resonances are a larger part of the overall response. Clearly more work on the modeling, and possibly on the fitting/convergence algorithms, is required to be able to fully understand the contributing $N^* \to K^+\Lambda$ states and to reconcile the results from the single-channel models with the currently available coupled-channel models.

VI. CONCLUSIONS

We have presented induced Λ polarization results for K^+ electroproduction for a total of 215 $(\cos\theta_K^{\text{c.m.}}, W)$ bins summed over Q^2 (at an average value of $Q^2 = 1.90$ GeV^2), covering the W range from threshold up to 2.7 GeV and the full kaon center-of-mass angular range. The induced polarization is uniformly negative, unlike the photoproduction data, which has kinematic areas of positive as well as negative polarization. The clear differences with the published CLAS photoproduction data at the mid and back kaon angles, where s-channel processes become important, emphasize that in studying electroproduction one can learn more about the contributing resonant and nonresonant terms. Furthermore, given the Q^2 independence observed in our data, there must be a dramatic change in the production process at lower momentum transfers. It is possible that future experiments using CLAS12 at Jefferson Lab may be able to probe this regime.

The data do not clearly indicate any obvious structures in the W dependence that one may interpret as indications of strong influences of s-channel resonances. However, there are large differences between the RPR-2011 model with and without resonances at back angles, indicating the importance of including such terms. The polarization data above $W = 2$ GeV at forward angles are reasonably well described by a nonresonant Regge mechanism, at least when comparing to the RPR-2007 model.

At the moment none of the available theoretical models can satisfactorily explain our results over the full kinematic range of the data. The predictions of RPR-2007 and the Extended Kaon-Maid model are in fair agreement with the experimental data at very forward kaon angles, but fare poorly when compared against the data in the rest of the kinematic phase space. The Maxwell model works well in the range $1.75 \leqslant W \leqslant 1.95$ GeV over most of the angular range, but is a poor match to the data elsewhere. The fact that RPR-2011NoL is generally better than the full RPR-2011 calculation indicates that the longitudinal response of the RPR-2011 model is off significantly. These findings are a strong indication that these data can be used to provide important constraints on future model fits, particularly when included within a fully coupled-channel partial-wave analysis. The sizable differences of the polarization results between the photo- and electroproduction data in the same W and $\cos\theta_K^{\text{c.m.}}$ range make clear that for a detailed understanding of the contributing resonant and nonresonant terms to the $K^+\Lambda$ final state, combined fits to both the photo- and electroproduction data will be essential. Additionally, measurements of $\mathcal{P}_N^0$ for the Σ^0 are also important for such fits because the Σ^0 provides access to additional intermediate states not accessible to the Λ. Specifically, it allows access to intermediate Δ and Δ^* states with isospin $3/2$ in addition to the isospin $1/2$ N^* states that are accessible to the Λ final state. Work is currently underway to extract $\mathcal{P}_N^0$ for the Σ^0 using these same data.

ACKNOWLEDGMENTS

We are grateful for the efforts of the staff of the Accelerator and Physics Divisions at Jefferson Lab that made this experiment possible. M. Gabrielyan was supported in part by a Florida International University Dissertation Year Fellowship. This work was supported in part by the Chilean Comisión Nacional de Investigación Científica y Tecnológica (CONICYT), the Italian Istituto Nazionale di Fisica Nucleare, the French Centre National de la Recherche Scientifique, the French Commissariat à l'Energie Atomique, the US Department of Energy, the National Science Foundation, the Scottish Universities Physics Alliance (SUPA), the United Kingdom's Science and Technology Facilities Council, and the National Research Foundation of Korea. The Southeastern Universities Research Association (SURA) operates the Thomas Jefferson National Accelerator Facility for the United States Department of Energy under Contract No. DE-AC05-06OR23177.

---

[1] I. Aznauryan *et al.*, Int. J. Mod. Phys. E **22**, 1330015 (2013).
[2] T. Mart, Int. J. Mod. Phys. E **19**, 2343 (2010).
[3] S. Capstick and W. Roberts, Prog. Part. Nucl. Phys. **45**, S241 (2000).
[4] H. Haberzettl, C. Bennhold, T. Mart, and T. Feuster, Phys. Rev. C **58**, R40 (1998).
[5] T. Mart and C. Bennhold, Phys. Rev. C **61**, 012201 (1999).

[6] B. Saghai, *Hadrons and Nuclei: First International Symposium*, AIP Conf. Proc. No. 594, edited by S.-W. Hong, I.-T. Cheon, T. Choi, and S. H. Lee (AIP, Melville, NY, 2001), p. 421.
[7] A. de la Puente, O. V. Maxwell, and B. A. Raue, Phys. Rev. C **80**, 065205 (2009).
[8] O. V. Maxwell, Phys. Rev. C **85**, 034611 (2012).
[9] O. V. Maxwell, Phys. Rev. C **86**, 064612 (2012).
[10] M. Guidal, J. M. Laget, and M. Vanderhaeghen, Nucl. Phys. A **627**, 645 (1997).
[11] M. Guidal, J. M. Laget, and M. Vanderhaeghen, Phys. Rev. C **61**, 025204 (2000).
[12] M. Guidal, J. M. Laget, and M. Vanderhaeghen, Phys. Rev. C **68**, 058201 (2003).
[13] T. Corthals, T. Van Cauteren, P. Vancraeyveld, J. Ryckebusch, and D. Ireland, Phys. Lett. B **656**, 186 (2007).
[14] L. DeCruz, T. Vrancx, P. Vancraeyveld, and J. Ryckebusch, Phys. Rev. Lett. **108**, 182002 (2012).
[15] A. Anisovich *et al.*, Eur. Phys. J. A **48**, 15 (2012).
[16] G. Penner and U. Mosel, Phys. Rev. C **66**, 055212 (2002).
[17] M. Döring, C. Hanhart, F. Huang, S. Krewald, U.-G. Meißner, and D. Rönchen, Nucl. Phys. A **851**, 58 (2011).
[18] H. Kamano, S. X. Nakamura, T. S. H. Lee, and T. Sato, Phys. Rev. C **81**, 065207 (2010).
[19] S. Capstick and W. Roberts, Phys. Rev. D **47**, 1994 (1993).
[20] M. Q. Tran *et al.* (SAPHIR Collaboration), Phys. Lett. B **445**, 20 (1998).
[21] S. Goers *et al.* (SAPHIR Collaboration), Phys. Lett. B **464**, 331 (1999).
[22] K. H. Glander *et al.* (SAPHIR Collaboration), Eur. Phys. J. A **19**, 251 (2004).
[23] R. G. T. Zegers *et al.*, Phys. Rev. Lett. **91**, 092001 (2003).
[24] M. Sumihama *et al.*, Phys. Rev. C **73**, 035214 (2006).
[25] H. Kohri *et al.*, Phys. Rev. Lett. **97**, 082003 (2006).
[26] A. Lleres *et al.* (GRAAL Collaboration), Eur. Phys. J. **31**, 79 (2007).
[27] A. D'Angelo *et al.* (GRAAL Collaboration), Eur. Phys. J. **31**, 441 (2007).
[28] A. Lleres *et al.* (GRAAL Collaboration), Eur. Phys. J. **39**, 149 (2009).
[29] J. W. C. McNabb *et al.* (CLAS Collaboration), Phys. Rev. C **69**, 042201(R) (2004).
[30] R. Bradford *et al.* (CLAS Collaboration), Phys. Rev. C **73**, 035202 (2006).
[31] R. Bradford *et al.* (CLAS Collaboration), Phys. Rev. C **75**, 035205 (2007).
[32] M. E. McCracken *et al.* (CLAS Collaboration), Phys. Rev. C **81**, 025201 (2010).
[33] B. Dey *et al.* (CLAS Collaboration), Phys. Rev. C **82**, 025202 (2010).
[34] J. Beringer *et al.* (Particle Data Group), Phys. Rev. D **86**, 010001 (2012).
[35] P. Ambrozewicz *et al.* (CLAS Collaboration), Phys. Rev. C **75**, 045203 (2007).
[36] R. Nasseripour *et al.* (CLAS Collaboration), Phys. Rev. C **77**, 065208 (2008).
[37] D. S. Carman *et al.* (CLAS Collaboration), Phys. Rev. C **87**, 025204 (2013).
[38] R. M. Mohring *et al.* (Hall C Collaboration), Phys. Rev. C **67**, 055205 (2003).
[39] G. Niculescu *et al.* (Hall C Collaboration), Phys. Rev. Lett. **81**, 1805 (1998).
[40] M. Coman *et al.* (Hall A Collaboration), Phys. Rev. C **81**, 052201 (2010).
[41] D. S. Carman *et al.* (CLAS Collaboration), Phys. Rev. Lett. **90**, 131804 (2003).
[42] D. S. Carman *et al.* (CLAS Collaboration), Phys. Rev. C **79**, 065205 (2009).
[43] G. Knöchlein, D. Drechsel, and L. Tiator, Z. Phys. A **352**, 327 (1995).
[44] B. A. Mecking *et al.*, Nucl. Instrum. Meth. A **503**, 513 (2003).
[45] M. D. Mestayer *et al.*, Nucl. Instrum. Meth. A **449**, 81 (2000).
[46] G. Adams *et al.*, Nucl. Instrum. Methods Phys. Res. A **465**, 414 (2001).
[47] E. S. Smith *et al.*, Nucl. Instrum. Methods Phys. Res. A **432**, 265 (1999).
[48] M. Amarian *et al.*, Nucl. Instrum. Methods Phys. Res. A **460**, 239 (2001).
[49] CLAS Physics Database, http://clasweb.jlab.org/physicsdb
[50] B. A. Raue and D. S. Carman, Phys. Rev. C **71**, 065209 (2005).
[51] T. Vrancx and J. Ryckebusch (private communication).
[52] T. Mart and L. Tiator (private communication).
[53] P. Achenbach, C. Ayerbe Gayoso, J. C. Bernauer, S. Bianchin, R. Böhm, O. Borodina, D. Bosnar, M. Bösz, V. Bozkurt, P. Bydžovský *et al.*, Eur. Phys. J. A **48**, 14 (2012).
[54] O. V. Maxwell (private communication).